



Characterization of spine and torso stiffness via differentiable biomechanics

Christos Koutras^a ^{*}, Hamed Shayestehpour^b , Jesús Pérez^a, Christian Wong^c,
John Rasmussen^b , Miguel A. Otaduy^a 

^a Universidad Rey Juan Carlos, Madrid, 28933, Spain

^b Aalborg University, Aalborg East, 9220, Denmark

^c University Hospital of Hvidovre, Hvidovre, 2650, Denmark

ARTICLE INFO

MSC:

49N45

65D18

65K10

Keywords:

Biomechanical modeling

Image-based estimation

Stiffness estimation

Scoliosis

Spine

ABSTRACT

We present a methodology to personalize the stiffness response of a biomechanical model of the torso and the spine. In high contrast to previous work, the proposed methodology uses controlled force–deformation data that mimic the conditions of spinal bracing for scoliosis, which leads to personalized biomechanical models that are suitable for computational brace design. The novel methodology relies on several technical contributions. First, a prototype system that includes controlled force measurement and low-dose radiographs, with low-encumbrance for its implementation in the clinical protocol. Second, a model of differentiable biomechanics of the torso and the spine, which becomes the key building block for robust parameter estimation. And third, an optimization procedure for parameter estimation from force–deformation data, which relies on differentiability of the biomechanics and the image generation process. We demonstrate the application of the methodology to a cohort of 7 subjects who underwent scoliosis check-ups, and we show quantitative validation of the estimated personalized parameters and the improvement over default parameters from the bibliography.

1. Introduction

1.1. Objective of the study

The development of personalized biomechanical models opens the door to advanced forms of computer-aided clinical design. One example, and the target application of our work, is computational design of spinal braces for adolescent idiopathic scoliosis (AIS). Spinal braces produce a correction on moderate cases of spine curvature during the period that it has a risk of progression and patients mature (Kaelin, 2020; Kuroki, 2018). Personalization of the braces can maximize effectiveness and satisfy comfort. While some works have explored the use of computer solutions for testing of brace designs (Wei et al., 2022; Guy et al., 2021; Cobetto et al., 2017; Vergari et al., 2020; Courvoisier et al., 2019), evaluation of bracing effectiveness as a function of biomechanical properties (Clin et al., 2010), or even for fully automated design as an optimization problem (Kardash et al., 2022), brace design remains mostly a manual process of trial and error. A major limiting factor for the adoption of computational brace design is the personalized characterization of the mechanical response, i.e., the stiffness, of the spine and torso of AIS patients.

Our initial hypothesis is that average stiffness values from the bibliography do not correctly capture the person-specific response of

the torso under typical bracing forces. To test this hypothesis, we estimate personalized spine and torso stiffness response, and compare spine deformations simulated under brace-like forces vs. those obtained with default stiffness values.

Unfortunately, previous methods for personalized stiffness characterization suffer important limitations, as we discuss below. Therefore, the bulk of our work was to develop a novel inverse-modeling methodology for spine and torso stiffness characterization.

1.2. Background: Mechanical modeling of the torso

Biomechanical modeling of the spine and torso has received much attention, and we point the reader to existing literature reviews for a broad coverage of existing works (Alizadeh et al., 2020; Knapik et al., 2022). Most of these works follow one of these two modeling approaches: Finite Element Modeling (FEM) of continuum elasticity or multi-body modeling.

Several surveys provide extensive discussion of FEM approaches (Wang et al., 2014; Wei et al., 2022; Naoum et al., 2021). The approach has been applied to both the cervical spine (Lasswell et al., 2017) and the lumbar spine (Dong et al., 2020; Xu et al., 2017). While these

* Corresponding author.

E-mail addresses: christos.koutras@urjc.es (C. Koutras), hs@mp.aau.dk (H. Shayestehpour), jesus.perez@urjc.es (J. Pérez), christian.nai.en.tierp-wong@regionh.dk (C. Wong), jr@mp.aau.dk (J. Rasmussen), miguel.otaduy@urjc.es (M.A. Otaduy).

<https://doi.org/10.1016/j.media.2025.103573>

Received 22 December 2022; Received in revised form 18 February 2025; Accepted 28 March 2025

Available online 19 April 2025

1361-8415/© 2025 The Authors. Published by Elsevier B.V. This is an open access article under the CC BY license (<http://creativecommons.org/licenses/by/4.0/>).

methods are potentially accurate, they require careful estimation of model parameters for personalized design applications. Nevertheless, various FEM models have been used in the computational design of scoliosis braces (Gignac et al., 2000; Nie et al., 2009).

Multi-body models offer a simpler and more efficient alternative. de Zee et al. (2007) developed a generic rigid-body model of the lumbar spine. Ignasiak et al. (2015), on the other hand, developed a multibody thoracolumbar spine model with an articulated rib cage. Shayesteh-pour et al. (2021) extended this work and presented an articulated spine and rib cage kinematic model, which attains scoliotic postures. Schmid et al. (2020) presented musculoskeletal full-body models, including the thoracolumbar spine, for children and adolescents. Bayoglu et al. (2019) developed a multibody musculoskeletal model of the human spine to study spinal loads. Favier et al. (2021) presented an open-source musculoskeletal model of the lumbar spine and lower limbs. Gould et al. (2021) and Jalalian et al. (2013) published two literature reviews of computational modeling of the spine, focusing on both the modeling approaches and the differences between healthy and scoliotic individuals.

There are also hybrid models, which try to combine the advantages of FEM and multi-body models. Dicko et al. (2015) developed a hybrid lumbar spine model which also supported contact mechanics. Koutras et al. (2021) developed a comprehensive model of the torso, representing the spine and the rib cage as a multi-body model, and the soft tissue with FEM. In our work, we build on this hybrid model.

1.3. Background: Spine model estimation

In multi-body spine modeling, much effort has been devoted to designing estimation procedures for the mechanical parameters of the models. The procedures can be classified as *in-vitro* or *in-vivo*. Research on stiffness characterization of the spine started with *in-vitro* experiments. Even though *in-vivo* methods are more suitable for model personalization, *in-vitro* methods still provide valuable insights, and their findings have significantly contributed to understanding the human spine. Furthermore, many existing models borrow their biomechanical parameters from *in-vitro* studies; in our case, we use them as default values and as starting point of our optimization.

Next, we discuss a selection of *in-vitro* parameter estimation procedures. Panjabi et al. (1976) estimated the rotational stiffness coefficients of the thoracic spine from experiments. They also estimated the translational stiffness coefficients of the thoracic spine through experimental studies, and later (Bisschop et al., 2012) followed this same line of work. In a different study, Panjabi et al. (1994) analyzed the mechanical behavior of the human lumbar and lumbosacral spine, as shown by three dimensional load–displacement curves performed *in-vitro*. Moroney et al. (1988) estimated the load displacement properties of the cervical spine; Liebsch et al. (2017, 2019) investigated the kinematic and stiffness properties of the thoracic spine and the rib cage; Wilke et al. (2017) examined the flexibility of every thoracic spinal segment; and Yamamoto et al. (2022) evaluated the biomechanical properties of the upper thoracic spine in anterior–posterior shear loading at various displacement rates. Zhang et al. (2020) completed a literature review about moment–rotation behavior of intervertebral joints on cadaveric tests. The review includes data from 1,648 intervertebral joints from 518 human cadavers in total.

We turn now to *in-vivo* parameter estimation procedures. *In vivo* procedures do not permit the application of localized deformations to the spine. Then, as spine stiffness is a heterogeneous property, its characterization is often reformulated as an inverse modeling problem, where the parameters of a spine and torso model are optimized to best fit full-torso deformation data.

Petit et al. (2004) developed a method to characterize the mechanical properties of the scoliotic spine using a flexible multi-body model and flexibility tests; Lafon et al. (2010) estimated the distribution of spinal intervertebral stiffness based on clinical flexibility

tests; Jalalian et al. (2017) presented a new method to approximate load–displacement relationships of spinal motion segments for patient-specific multi-body models of scoliotic spine based on flexibility tests; and Wang et al. (2021) used a dynamic optimization approach for solving spine kinematics while calibrating subject-specific mechanical properties of 10 healthy subjects, based on skin-mounted markers. Guy and Aubin (2023) estimate spine stiffness to match the spine deformation produced by in-brace correction. None of the aforementioned studies (and more in the literature) use external force data as part of the estimation procedure; they depend solely on displacement data. Thus, as discussed also by other authors (Berger et al., 2015), they can only estimate relative stiffnesses up to a scale factor, they cannot estimate the absolute stiffness response. Correct calibration of stiffness is necessary, for instance, for the estimation of bracing forces and the evaluation of comfort in brace design.

Some works have addressed the estimation of spine stiffness from force–displacement relationships. Affolter et al. (2020) predicted the flexion–extension stiffness responses of a lumbar functional spine unit (FSU) modeled with subject-specific FEM from *in-vivo* 6-degree-of-freedom (DoF) kinematics. Their method is based on dynamic stereo x-ray imaging of a functional lifting task. While their estimation leverages a force–deformation relationship, it contains only flexion/extension experiments for one FSU; therefore, it does not support the parameterization of a full torso model for scoliosis brace design. Qiao and Rahmatalla (2020) identified the damping and stiffness parameters of cervical and lumbar spine of supine humans using modal analysis under vertical whole-body vibration. Unfortunately, due to the type of motion used in the experiments, the resulting parameters do not correctly represent the motions occurring under scoliosis bracing. Ghezlbash et al. (2016) developed a computational musculoskeletal trunk model that can be personalized using a scaling scheme, and Eskandari et al. (2017) proposed an image-based kinematics measurement approach to develop subject-specific musculoskeletal models. These models correspond to healthy individuals and do not account for scoliosis peculiarities. Berger et al. (2015) developed a method for preoperative stiffness characterization based on a force–displacement relationship. However, their method requires a special platform (Büchler et al., 2014) and their boundary conditions are not similar to those in bracing. Park et al. (2018) used a robotic spine exoskeleton and characterized the three-dimensional stiffness of the torso by a 6×6 stiffness matrix. Murray et al. (2020) extended their method to scoliosis patients. Despite their contributions, their methodology suffers several limitations: the robotic exoskeleton complicates implementation in the clinical protocol for AIS patients; the acquired data lacks imaging data that depicts the detailed deformation of the spine, it contains only deformations of the outer torso; and they estimate only a 6×6 stiffness matrix for the full torso, which does not correctly capture the deformation response to bracing.

1.4. Background: Adjoint method for mechanical model estimation

The adjoint method is a standard mathematical tool to efficiently compute gradients of optimization functions, by traversing the chain rule of derivatives in a convenient order (Lions, 1971). In inverse design problems, the design objective function depends on both design parameters and state DoFs. Differential changes to design parameters can be related to differential changes to state DoFs through a sensitivity matrix, but the adjoint method enables the efficient computation of the gradient of the design objective with respect to design parameters, without explicitly computing the sensitivity matrix.

The adjoint method has been used for various stiffness estimation problems formulated from force–deformation data. Examples include the estimation of constitutive elastic parameters in solid mechanics (Bickel et al., 2009), and the estimation of elasticity parameters in cloth (Miguel et al., 2012). Our work follows a similar methodology, and we show how to formulate a differentiable biomechanics model of the torso, for robust and efficient application of the adjoint method.

Beyond inverse design, the adjoint method has been applied to many other computational design problems. Some examples include animation control (McNamara et al., 2004; Wojtan et al., 2006), 3D printing (Pérez et al., 2015, 2017), ergonomics design (Zhao et al., 2022), or even scoliosis brace design (Kardash et al., 2022), which could leverage our model personalization methodology.

2. Methods: Acquisition of spine deformations and forces

The first central ingredient of our inverse-modeling methodology for stiffness characterization is a novel data acquisition procedure. The acquisition of force and deformation data suitable for the characterization of spine and torso biomechanical models faces two major challenges. One is the acquisition of deformations under known forces that are representative of the conditions imposed by AIS bracing. Another one is the design of simple, low-radiation procedures, which can be easily adopted in the standard patient check-up procedures.

In this section, we describe our measurement setup, as well as the acquisition of deformation and force data for our estimation algorithm. Our prototype measurement setup and procedure enables the acquisition of multiple low-dose radiographs while applying controlled forces to the subject. This setup and procedure fulfills competing goals. On one hand, it produces controlled deformation and force data, suitable for stiffness characterization, and the deformation data mimics the correcting effect of scoliosis bracing. On the other hand, it is performed without discomfort for patients and induces minimal radiation (Wong et al., 2021), favoring its potential adoption in regular check-up procedures.

2.1. Description of the setup and procedure

To capture spine deformations while minimizing radiation, we obtain a series of low-dose radiographs. Specifically, we used a DelftDI D2RS system with fluoroscopic exposure. This device emits around one-eighth of the radiation of standard x-rays (Wong et al., 2021). The following acquisition parameters were assessed: tube potential (71 kVp, density set at 0), with grid, using automated mA selection exposure control and additional filtration (1 mm Al + 0,1 mm Cu). The pixel size was 0.139 mm with a maximum resolution of 3.6 lp/mm.

To produce spine deformations similar to the ones produced by scoliosis braces, we mimic the three-point pressure principle as applied by, e.g., Rigo Chêneau-type braces (Rigo and Jelačić, 2017). Specifically, we apply a force on the ribs on one side of the subject, while keeping the pelvis and the opposite shoulder fixed. The rib force is applied through a Sauter FH500 force gauge (which can accurately measure forces up to 500 N), thus providing a measurement of the applied force at every time. The pelvis and the shoulder are fixed by using a fixing belt and asking the subject to rest the shoulder on a rigid wall attached to the x-ray bed. The pelvis support acts as the main support point below the applied force to prevent bending of the torso, and for this reason the horizontal forces at the feet are minimal. The complete setup can be seen in Fig. 1. The back of the subject is in contact with the vertical wall of the x-ray bed to avoid torsion of the torso. At the same time, as the x-ray bed is smooth, friction forces against the back are minimal. Altogether, the setup produces three relevant forces on the user on the frontal plane: F_1 on the shoulder, F_2 on the pelvis, and F_3 on the ribs, as shown in Fig. 1. These three forces resemble the three-point pressure system and produce the desired deformations.

The measurement procedure consisted of applying a growing rib force on each side of the subject's torso, while recording a series of radiographs. The recording of radiographs and force measurements were synchronized. For each side, we captured four to eight radiographs, up to a maximum force of 114 N, at a rate of four radiographs per second. Subjects were instructed to remain calm and breathe normally, and communicate if the force became uncomfortable; for this reason the procedure was stopped early in some cases.

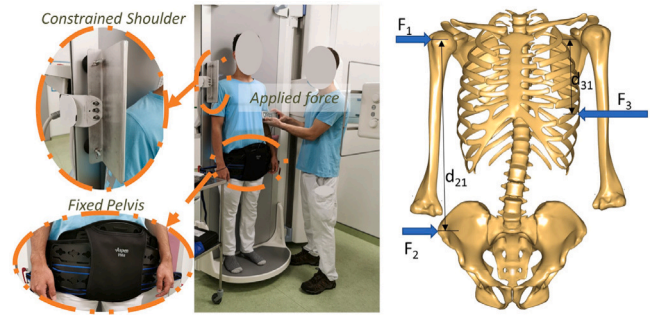


Fig. 1. Photographs and schematic depiction of the experimental force-and-deformation acquisition setup. We capture low-dose radiographs of the subject's torso while simultaneously increasing a controlled force (F_3) on the ribs. This force is balanced by a force on the opposite shoulder (F_1) obtained by resting the shoulder against a wall attached to the x-ray bed (see top-left inset), and a force on the pelvis (F_2) produced by a fixing belt (see bottom-left inset). The three forces together resemble the three-point pressure principle of common scoliosis braces. Using force and torque equilibrium conditions, together with body measurements d_{21} and d_{31} , we estimate the reaction forces on the shoulder and the pelvis.

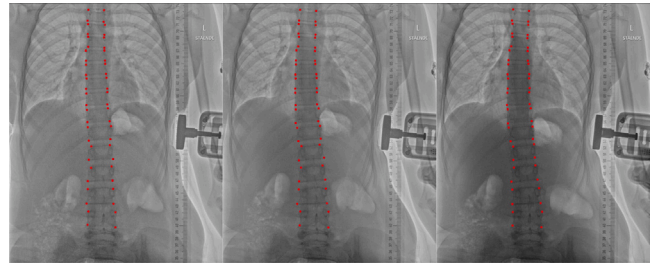


Fig. 2. A sequence of three radiographs of a subject under increasing rib force (from left to right). The red dots depict the tracked vertebra features used in our estimation algorithm.

For the estimation process described later in Section 4, we decided to keep only three radiographs per subject (and their corresponding force measurements), two used for estimation and one for validation (see Fig. 2). We selected the measurements of highest quality, both in terms of image quality and no motion of the shoulder or the pelvis, with the force applied on the same side of the torso in all three images. For some subjects, the selected images correspond to a decreasing scoliosis curve, while for other subjects they correspond to an increasing curve. The described radiographs were complemented with rest-state frontal and lateral radiographs used for the personalization of the torso geometry, following the procedure described in Koutras et al. (2022).

Our experimental setup is only a research prototype for designing a complete measurement and biomechanical estimation procedure. In future work, it would be convenient to optimize the procedure and the acquisition setup to maximize biomechanical estimation accuracy while minimizing the number of required radiographs.

2.2. Tracking deformation features on radiographs

To estimate the parameters of the torso biomechanics model, it is necessary to correlate the deformation of the simulated torso (i.e., the positions and orientations of bones) to the deformation captured in the radiographs. For this purpose, on each radiograph (with subindex j), we define as deformation features the corners (with subindex k) of each vertebral bone $\{\hat{c}_{j,k}\}$. These features characterize the 2D position and orientation of the vertebrae as explained later in Section 4.1.

Identifying the features of each vertebra in all radiographs is a challenging task. Manual annotation in all x-rays would require a considerable amount of manual work, and it would be subject to annotation accuracy errors. Instead, we manually annotated the features

in one radiograph for each subject, and then we used an optical flow algorithm to track the features in the rest of the images. Examples of tracked vertebra features can be seen in Fig. 2.

Our tracking algorithm works incrementally with pairs of images, starting from the initial annotated radiograph. Given two images, one already annotated and one not, we first match the histograms of both images (Bradski, 2000), and then use an optical flow algorithm (Bradski, 2000) to transform the features to the new image. We do the same with the next image in the sequence until the complete sequence is annotated.

2.3. Force measurements

All three forces F_1 , F_2 and F_3 are used as input boundary conditions to our biomechanics model estimation. However, for simplicity of the measurement setup, only F_3 is actively measured. Fortunately, we can leverage force and torque equilibrium conditions on the frontal plane to infer F_1 and F_2 .

As illustrated in Fig. 1, we measure the vertical distances d_{21} between the shoulder and the pelvis, and d_{31} between the shoulder and the ribs. Then, we can formulate torque equilibrium with respect to the shoulder, as well as force equilibrium, to obtain the shoulder and pelvis forces F_1 and F_2 :

$$d_{21} F_2 - d_{31} F_3 = 0 \quad \Rightarrow \quad F_2 = \frac{d_{31}}{d_{21}} F_3. \quad (1)$$

$$F_1 + F_2 - F_3 = 0 \quad \Rightarrow \quad F_1 = \frac{d_{21} - d_{31}}{d_{21}} F_3. \quad (2)$$

3. Methods: Differentiable biomechanics of the Torso

The second central ingredient of our inverse-modeling methodology for stiffness characterization is a differentiable model of spine and torso biomechanics. We have developed a biomechanical model that predicts the deformation of the torso under external forces comparable to those of a scoliosis brace. Furthermore, thanks to a differentiable formulation of the biomechanics simulation, we can define an inverse mapping from torso deformation to model parameters, which will be key in our parameter estimation process. This section starts by describing the components of the biomechanics model, follows with the formulation of biomechanical simulation, and concludes by discussing the differentiability of the simulation.

3.1. Biomechanical model of the Torso

Biomechanical models of the torso may be designed with different granularity depending on the forces and deformations under study. Here, we are concerned with predicting the passive deformation of the torso skeleton under external forces similar to those applied by a scoliosis brace. To this end, we consider the multi-body system formed by the skeletal bones as rigid bodies connected by joints. The surrounding soft tissue (skin, muscles and organs) has an important effect in capturing the deformation stiffness of the torso (Koutras et al., 2021), and in particular in preserving a smooth deformation of the rib cage (Koutras et al., 2022); therefore, it is also included in our model. However, for scoliosis brace design, we consider the torso passive, i.e., without active muscle forces, as this condition can be considered an approximate average of muscle activity. We build on the model proposed by Koutras et al. (2021), with an extension to the shoulders, the collarbone and the scapulae, to correctly map the shoulder force to the spine.

We model the torso skeleton with all lumbar and thoracic vertebrae, the rib cage, the sternum, the pelvis, the scapulae, the collarbone, and the proximal ends of the humeri as rigid bodies. We connect the bones through 6D compliant joints, which gather the complex effects that exist in reality. Following Koutras et al. (2021), each 6D joint contributes an energy $E_{\text{joint},i} = \frac{1}{2} \Delta \mathbf{x}_i^T \text{diag}(\mathbf{k}_{x,i}) \Delta \mathbf{x}_i + \frac{1}{2} \Delta \theta_i^T \text{diag}(\mathbf{k}_{\theta,i}) \Delta \theta_i$,

Table 1

Default stiffness values (in kN/m for translation, N/rad for rotation) for the various 6D joints in our model.

Joint stiffnesses	\bar{k}_x	\bar{k}_y	\bar{k}_z	\bar{k}_α	\bar{k}_β	\bar{k}_γ
Thoracic segment	262	1720	262	154	137	154
Lumbar segment	245	1720	245	143	498	149
Rib-vertebrae	53.9	123	123	9.7	6.87	6.87
Rib-sternum	51.85	8	8	9.7	2.29	2.29
Sternum-clavicle	10^4	10^4	10^4	10^4	1	1
Clavicle-scapula	10^4	10^4	10^4	1	1	1
Scapula-humerus	10^4	10^4	10^4	1	1	1

where $\Delta \mathbf{x}_i$ is the translation displacement of the joint, $\Delta \theta_i$ is the rotation displacement (expressed as an axis-angle product), and $\mathbf{k}_{x,i}$ and $\mathbf{k}_{\theta,i}$ are anisotropic translation and rotation stiffness values for each joint axis. All quantities are computed in each joint's local frame. As discussed by Koutras et al. the 6D intervertebral joints represent the compound effect of intervertebral disks, ligaments, and facet joints; the 6D joints between ribs and vertebrae gather the effect of both the costo-vertebral and costo-transverse joints, which in turn consist of the capsules and the surrounding ligaments; and the 6D joints between ribs and sternum gather the effect of the costal cartilages and the costo-sternal joints. These simplifications are suitable for the analysis of bracing deformations of the spine (Ignasiak et al., 2015).

We consider the surface of the torso surrounding the skeleton, clipped between the neck and the waist, and we model the underlying soft tissue using an FEM discretization of a Neo-Hookean material with elastic energy density $\Psi = \frac{\mu}{2} (I_1 - 3) - \mu \log J + \frac{\lambda}{2} (\log J)^2$ (Ogden, 1997; Sifakis and Barbic, 2012; Smith et al., 2018). To mesh the soft tissue, we input the torso surface along with spatially distributed sample points on the surfaces of the bones, and we create a conformal tetrahedral mesh (Hang, 2015). The points on the surfaces of the bones define the coupling between skeletal bones and soft tissue.

Let us define a vector of DoFs of the torso model, \mathbf{x} , which concatenates the positions of soft-tissue mesh nodes and the translations and rotations of all bones (with rotations modeled using the incremental rotation-vector representation (Taylor and Kriegman, 1994)). From these DoFs, the rest configuration of the torso, the mechanical parameters of the model \mathbf{k} , and the applied external forces \mathbf{f}_{ext} , we define biomechanical energies that characterize the deformation of the torso. In particular, we consider three energy terms:

- The elastic energy of the joints between bones, $E_{\text{joints}}(\mathbf{x}, \mathbf{k})$.
- The elastic energy of the soft tissue, $E_{\text{tissue}}(\mathbf{x}, \mathbf{k})$.
- The mechanical work produced by external forces, $E_{\text{ext}}(\mathbf{x}, \mathbf{f}_{\text{ext}}) = -\mathbf{f}_{\text{ext}}^T \mathbf{x}$. The external forces include the shoulder force F_1 applied on the proximal end of the humerus, the pelvis force F_2 , and the rib force F_3 distributed on the two ribs closest to the location of the force.

As mentioned above, we build this model starting from the model proposed by Koutras et al. (2021), and we refer the reader to their work for full details on the definition of the joints, their parameterization and energy model, as well as the soft-tissue model. We extend their model with key anatomical elements necessary for transferring the shoulder force to the spine. Specifically, they consist of the scapulae, the collarbone, and the heads of the humeri, as well as the joints connecting these elements. We add ball-and-socket joints between scapulae and humeri, scapulae and the collarbone, and the sternum and the collarbone. In the latter case, we also constrain the rotation along the mediolateral axis, following the model in Rasmussen (2019).

Our choice of model parameterization also follows the work of Koutras et al. (2021). We choose the default joint-stiffness and soft-tissue parameters defined in their work, summarized for completeness in Table 1. We also include the default stiffness values for the new joints added in our model, which are set as very high stiffness for constrained

directions and very low stiffness for unconstrained directions. In the notation of stiffness parameters, for intervertebral joints the Y axis defines separation (k_y) and axial rotation (k_β), the X axis defines lateral translation (k_x) in the frontal plane and flexion/extension in the sagittal plane (k_α), and the Z axis defines sagittal translation (k_z) and lateral bending (k_γ). For other joints, the X axis defines separation (k_x) and axial rotation (k_α), and the other two axes are chosen arbitrarily on the orthogonal plane, as they are isotropic.

However, since the parameters do not share a common scale, Koutras et al. propose a reparameterization based on parameter ratios for parameter analysis and/or estimation. Each parameter k_i is defined as $k_i = \xi_i \bar{k}_i$, where \bar{k}_i is the default parameter value and ξ_i is the parameter ratio. The vector of model parameters \mathbf{k} is defined by concatenating all parameter ratios under study. Later in Section 4.3 we discuss what parameters exactly we estimate.

The purpose of our work is to personalize the biomechanical model for each subject, to correctly capture the mechanical response under external forces. However, prior to this, and relying on existing methods (Koutras et al., 2022), we personalize the geometry of the torso model. We start from a template geometry, and we optimize the match to rest-state frontal and lateral low-dose radiographs, together with a biomechanically inspired regularization.

3.2. Static equilibrium solver

According to the energy terms defined previously, the total energy of the biomechanical model of the torso is

$$E = E_{\text{joints}}(\mathbf{x}, \mathbf{k}) + E_{\text{tissue}}(\mathbf{x}, \mathbf{k}) + E_{\text{ext}}(\mathbf{x}, \mathbf{f}_{\text{ext}}). \quad (3)$$

Given a set of mechanical parameters \mathbf{k} , we want to predict the deformation of the torso produced by the external forces. We do this by solving a static equilibrium problem, which is equivalent to minimizing the total energy of the model:

$$\mathbf{x}(\mathbf{k}, \mathbf{f}_{\text{ext}}) = \arg \min_{\mathbf{x}} E(\mathbf{x}, \mathbf{k}, \mathbf{f}_{\text{ext}}). \quad (4)$$

It follows that the minimum-energy configuration can be expressed as a zero-net-force constraint on the DoFs:

$$\mathbf{f}(\mathbf{x}, \mathbf{k}, \mathbf{f}_{\text{ext}}) = \mathbf{f}_{\text{joints}}(\mathbf{x}, \mathbf{k}) + \mathbf{f}_{\text{tissue}}(\mathbf{x}, \mathbf{k}) + \mathbf{f}_{\text{ext}} = 0. \quad (5)$$

To solve the minimization problem, we use Newton's method with line search (Wright et al., 1999). On every Newton's iteration, we compute the Jacobian of the forces, which corresponds to the negative Hessian of the energy, we solve a linear system for the change in the DoFs, and we take a step that minimizes energy. Our model is implemented in C++, and we solve the linear systems with the conjugate gradient method using Eigen (Guennebaud et al., 2010).

3.3. Differentiable biomechanics

To estimate model parameters, we require a sensitivity matrix that provides a differential mapping from model parameters \mathbf{k} to model DoFs \mathbf{x} . We obtain this sensitivity matrix $\frac{\partial \mathbf{x}}{\partial \mathbf{k}}$ efficiently thanks to our differentiable biomechanics formulation.

From the zero-net-force constraint (5), we apply the implicit function theorem to obtain:

$$\frac{\partial \mathbf{f}}{\partial \mathbf{x}} \frac{\partial \mathbf{x}}{\partial \mathbf{k}} + \frac{\partial \mathbf{f}}{\partial \mathbf{k}} = 0 \quad \rightarrow \quad \frac{\partial \mathbf{x}}{\partial \mathbf{k}} = -\frac{\partial \mathbf{f}}{\partial \mathbf{x}}^{-1} \frac{\partial \mathbf{f}}{\partial \mathbf{k}}. \quad (6)$$

In practice, the sensitivity matrix is used to back-propagate gradients on DoFs \mathbf{g} to gradients on parameters as $\frac{\partial \mathbf{x}}{\partial \mathbf{k}}^T \mathbf{g}$. This is done efficiently using the adjoint method:

$$\frac{\partial \mathbf{x}}{\partial \mathbf{k}}^T \mathbf{g} = -\frac{\partial \mathbf{f}}{\partial \mathbf{k}}^T \mathbf{u}, \quad \text{with} \quad \frac{\partial \mathbf{f}}{\partial \mathbf{x}} \mathbf{u} = \mathbf{g}. \quad (7)$$

The only costly operation corresponds to solving a linear system $\frac{\partial \mathbf{f}}{\partial \mathbf{x}} \mathbf{u} = \mathbf{g}$, but the force Jacobian $\frac{\partial \mathbf{f}}{\partial \mathbf{x}}$ is readily available from the equilibrium solve described above in Section 3.2.

We compute analytically the Jacobian of forces with respect to parameters, $\frac{\partial \mathbf{f}}{\partial \mathbf{k}}$, and to this end we extend the underlying biomechanics simulator. Specifically, we require Jacobians of joint forces $\mathbf{f}_{\text{joints}}$ with respect to joint stiffness ratios, and Jacobians of soft-tissue forces $\mathbf{f}_{\text{tissue}}$ with respect to Lamé parameter ratios. Each joint force is computed as $\mathbf{f}_{\text{joints},i} = \xi_i \hat{\mathbf{f}}_{\text{joints},i}$, where ξ_i is the joint stiffness ratio and $\hat{\mathbf{f}}_{\text{joints},i}$ is the joint force with the default stiffness value. Then, the force Jacobian with respect to the stiffness ratio is trivially obtained as $\frac{\partial \mathbf{f}_{\text{joints},i}}{\partial \xi_i} = \hat{\mathbf{f}}_{\text{joints},i}$. Soft-tissue forces due to the Neo-Hookean material (see Section 3.1) can be seen as the superposition of two force terms linear with respect to each Lamé parameter. Accounting for the parameter ratios ξ_μ and ξ_λ , the soft-tissue forces can then be expressed as $\mathbf{f}_{\text{tissue}} = \xi_\mu \hat{\mathbf{f}}_\mu + \xi_\lambda \hat{\mathbf{f}}_\lambda$, with $\hat{\mathbf{f}}_\mu$ and $\hat{\mathbf{f}}_\lambda$ the soft-tissue force terms with default Lamé parameters. Then, the force Jacobians with respect to the Lamé parameter ratios are trivially $\frac{\partial \mathbf{f}_{\text{tissue}}}{\partial \xi_\mu} = \hat{\mathbf{f}}_\mu$ and $\frac{\partial \mathbf{f}_{\text{tissue}}}{\partial \xi_\lambda} = \hat{\mathbf{f}}_\lambda$.

4. Methods: Optimization-based stiffness estimation

The third and final central ingredient of our inverse-modeling methodology for stiffness characterization is an optimization-based approach for the estimation of spine and torso stiffness parameters. In a nutshell, we search for the torso and spine stiffnesses that minimize image-space error of the spine deformation with respect to the input radiographs.

We start this section describing the exact formulation of the optimization problem. Then we describe the solution of the optimization problem with robust gradient-based methods. To this end, we model the complete transformation from biomechanical parameters to image features as a differentiable process. This includes the differentiable biomechanics model, as well as differentiation of the transformation to image features. We follow with a discussion of the choice of stiffness parameters that we optimize. In choosing these parameters, we leverage problem-specific knowledge provided by the optimization gradients, which ensures robust parameter estimation. We conclude the section with a short note on performance.

4.1. Optimization problem

We formulate the estimation of stiffness parameters \mathbf{k} as the minimization of image-space error of spine deformation, subject to force-equilibrium constraints in the biomechanics. We define an image-space error per target radiograph, $\mathcal{L}(\mathbf{x}_j, \hat{\mathbf{c}}_j)$, based on the torso and spine deformation \mathbf{x}_j and the image features $\hat{\mathbf{c}}_j$ for each particular radiograph (See Section 2.2). Similarly, we express force-equilibrium constraints as in (5) per target radiograph, based again on the torso and spine deformation, the stiffness parameters, and the external forces $\mathbf{f}_{\text{ext},j}$ for each radiograph. Formally, the complete optimization problem of the objective function $f(\mathbf{k})$ can be expressed as the following constrained optimization:

$$\mathbf{k} = \arg \min_{\mathbf{k}} f(\mathbf{k}) \rightarrow \quad (8)$$

$$\mathbf{k} = \arg \min_{\mathbf{k}} \sum_j \mathcal{L}(\mathbf{x}_j, \hat{\mathbf{c}}_j), \quad \text{s.t. } \mathbf{f}(\mathbf{x}_j, \mathbf{k}, \mathbf{f}_{\text{ext},j}) = 0, \forall j.$$

Next, we detail the definition of the objective function term for each radiograph. Given N tracked vertebrae with their corresponding 4 image features $\hat{\mathbf{c}}_{j,k}$, $k \leq 4N$, we transform these to robust geometric features $\hat{\mathbf{z}}_{j,k}$, and we compute their image-space error with respect to corresponding geometric features $\mathbf{z}_k(\mathbf{x}_j)$ computed from the torso deformation \mathbf{x}_j :

$$\mathcal{L}(\mathbf{x}_j, \hat{\mathbf{c}}_j) = \frac{1}{2} \sum_{k \leq 4N} \left| \hat{\mathbf{z}}_{j,k}(\hat{\mathbf{c}}_j) - \mathbf{z}_k(\mathbf{x}_j) \right|^2. \quad (9)$$

The computation of image-space errors could be approached by defining correspondences between the image features $\hat{\mathbf{c}}_{j,k}$ and 3D points on the vertebrae model, transforming these 3D points according to

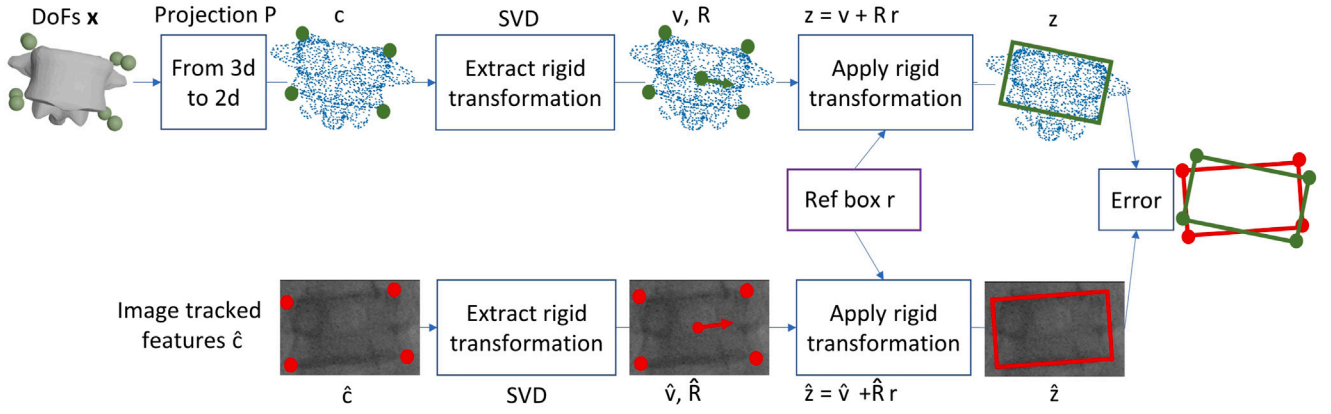


Fig. 3. This pipeline depicts the computation of image-space deviation between image features tracked on radiographs (bottom) and spine simulation results (top). We use as error metric the distances between the corners of a reference 2D box representing each vertebra, due to the lack of accurate correspondences between the simulated vertebrae and the tracked image features. On top, the box is transformed using a 2D rigid transformation extracted from the projection of each simulated vertebra. At the bottom, the box is transformed using a 2D rigid transformation extracted from the tracked image features.

the spine deformation, projecting the 3D points to 2D image space, and finally measuring 2D errors. Unfortunately, it is not possible to define accurate 3D correspondences for the image features due to three major reasons. First, the 3D models of the vertebrae are obtained from a template model (see Koutras et al., 2022), and their geometry is not personalized. Second, the image features are initialized through a manual annotation process. And third, the image features track the corners of the projected silhouettes of the vertebrae, but not necessarily fixed points on the vertebrae. For these reasons, we transform the image features to more robust geometric features, and then we can define explicit correspondences with the 3D models of the vertebrae. Fig. 3 shows a schematic outline of the error computation procedure per vertebra, using as inputs the image features and the vertebra transformation, and mediated through the robust geometric features.

Our process for defining robust geometric features considers a reference 2D bounding box per vertebra, and the corners of this box are transformed using separately the image features (to yield $\hat{z}_{j,k}(\hat{c}_j)$) and the spine deformation (to yield $z_k(x_j)$). We use the image features or the spine deformation to define the 2D transformations of the reference box, but not the geometric features directly, thus making the process robust. We initialize the reference 2D box by first computing the 3D oriented bounding box per vertebra (using the template model), and simply aligning the width and height of the 3D box with the 2D axes, i.e., we discard the depth and orientation of the vertebra. We define as $r_k, k \leq 4N$, the corners of the reference boxes.

To compute target geometric features $\hat{z}_{j,k}$ per vertebra, we proceed as follows. First, we identify the center of mass $\hat{v}_{j,v} = \frac{1}{4} \sum_{k \in v} \hat{c}_{j,k}$ and the best-fit orientation $\hat{R}_{j,v}$ of the four image features of the vertebra. Here, v denotes the vertebra. We compute $\hat{R}_{j,v(k)}$ by first obtaining the covariance matrix of the image features, $\hat{C}_{j,v} = \frac{1}{4} \sum_{k \in v} (\hat{c}_{j,k} - \hat{v}_{j,v})(\hat{c}_{j,k} - \hat{v}_{j,v})^T$; and then its singular value decomposition (SVD) $\hat{C}_{j,v} = \hat{R}_{j,v} \hat{\Sigma}_{j,v} \hat{R}_{j,v}^T$. Finally, we use the resulting rigid transformation to transform the corners of the reference box, and we obtain the target geometric features, $\hat{z}_{j,k} = \hat{v}_{j,v} + \hat{R}_{j,v} r_k$.

To compute simulation geometric features $z_k(x_j)$, we follow a similar approach. We start from the corners ${}_3r_k$ of the 3D oriented bounding box of a vertebra, we transform them according to the vertebra transformation (with translation ${}_3v_{j,v}$ and rotation ${}_3R_{j,v}$), and then project them with the projection matrix P of the x-ray system, to obtain 2D corners $c_{j,k} = P({}_3v_{j,v} + {}_3R_{j,v} {}_3r_k)$. Out of the eight 2D corners, we pick four that define the visible silhouettes of the top and bottom plates of the vertebra. We do this by selecting one corner from each corresponding pair of front and back corners of the vertebra box. We end with four image-space features $\{c_{j,k}\}$ per vertebra, and the rest of the process is analogous to the computation of geometric features from

the image features. We compute the center of mass $v_{j,v} = \frac{1}{4} \sum_{k \in v} c_{j,k}$, the covariance matrix $C_{j,v} = \frac{1}{4} \sum_{k \in v} (c_{j,k} - v_{j,v})(c_{j,k} - v_{j,v})^T$, and the best-fit orientation through the SVD $C_{j,v} = R_{j,v} \Sigma_{j,v} R_{j,v}^T$. Then we transform the corners of the reference box to obtain the simulation geometric features, $z_{j,k} = v_{j,v} + R_{j,v} r_k$.

In the objective function (8), we measure error for all N tracked vertebrae on each radiograph, as denoted in (9). Ideally, we would pick all 17 thoracic and lumbar vertebrae on all radiographs, as those possibly involved in scoliosis and affected by brace forces. However, because of the limited width and height of the low-dose x-ray machine, not all 17 thoracic and lumbar vertebra are visible in the target radiographs for all subjects. As a result, in practice we pick N to be the visible vertebra of each subject. $N \in [13, 17]$ in practice.

4.2. Gradient and solver

We have used the L-BFGS-B optimization algorithm (Nocedal and Wright, 2006), in its scipy implementation in Python (Virtanen et al., 2020) to optimize the problem in (8). To this end, we have generated Python bindings of the C++ biomechanical simulation. L-BFGS-B evaluates the objective function on each iteration step, then uses gradient evaluations to approximate the Hessian in a Newton-like algorithm, and takes a step that reduces the objective. Every time a step is taken, it is necessary to solve the static equilibrium of the torso on all radiographs. Note that the differentiable biomechanics model can only be applied if the force-equilibrium constraint is satisfied.

The gradient of the objective function in (8) with respect to the model parameters k can be expressed as:

$$\frac{\partial f}{\partial k} = \sum_j \frac{\partial x_j}{\partial k} \frac{\partial \mathcal{L}(x_j, \hat{c}_j)}{\partial x_j} \quad (10)$$

Following the differentiable biomechanics formulation from Section 3.3, each product $\frac{\partial x_j}{\partial k} \frac{\partial \mathcal{L}(x_j, \hat{c}_j)}{\partial x_j}$ can be computed by propagation through the simulation model as in (7), with $g = \frac{\partial \mathcal{L}(x_j, \hat{c}_j)}{\partial x_j}$, the gradient of each error term with respect to the simulation DoFs.

Obtaining the gradients of the error terms requires differentiating the complete error computation process described above in Section 4.1, which can be summarized as: $({}_3v_{j,v}, {}_3R_{j,v}) \rightarrow c_k \rightarrow (v_v, C_v \rightarrow R_v) \rightarrow z_k \rightarrow \mathcal{L}$. We apply the chain rule to this process, to obtain error gradients with respect to vertebra translation ${}_3v_{j,v}$ and vertebra rotation ${}_3R_{j,v}$. In the following expression, w denotes either ${}_3v_{j,v}$ or ${}_3R_{j,v}$.

$$\frac{\partial \mathcal{L}}{\partial w} = \sum_{k \in v} (\hat{z}_{j,k}(\hat{c}_j) - z_k(x_j))^T \frac{\partial z_k}{\partial w} \quad (11)$$

Table 2

This table indicates the main characteristics of each participant (age, gender, height, Cobb angle of the spine, and scoliosis curve type), as well as summarized information about the captured measurements (maximum change of Cobb angle produced during data capture, and maximum applied force). A positive sign of Cobb angle indicates left curvature (which is the majority condition), and negative sign indicates right curvature. Similarly, a positive force indicates pushing toward left curvature, and negative force indicates pushing toward right curvature. Average Cobb angle and maximum force were computed using absolute values, regardless of curvature direction.

Subject characteristics	# 1	# 2	# 3	# 4	# 5	# 6	# 7	Average (abs)
Age	11	15	10	12	15	10	14	12.4
Gender	female	female	male	female	female	male	male	–
Height (cm)	157	160	144	146	168	139	165	154
Init Cobb (deg)	+11	+16	+15	–10	+16	+11	+7	12.3
Scoliosis Curve	Thoracic	Lumbar	Thoracic	Thoracic	Lumbar	Thoracolumbar	Thoracic	–
Change Cobb (deg)	–19	+13	–46	+25	+8	–26	–20	22.4
Max force (N)	–59	+114	–60	+79	+88	–45	–92	76.7

$$\frac{\partial \mathbf{z}_k}{\partial \mathbf{w}} = \sum_{l \in v} \left(\frac{\partial \mathbf{z}_k}{\partial \mathbf{v}_v} \frac{\partial \mathbf{v}_v}{\partial \mathbf{c}_l} + \frac{\partial \mathbf{z}_k}{\partial \mathbf{R}_v} \frac{\partial \mathbf{R}_v}{\partial \mathbf{C}_v} \frac{\partial \mathbf{C}_v}{\partial \mathbf{c}_l} \right) \frac{\partial \mathbf{c}_l}{\partial \mathbf{w}}. \quad (12)$$

The majority of the derivatives are trivial to compute, as the process of computing the error involves mostly simple arithmetic. The only complex term is $\frac{\partial \mathbf{R}_v}{\partial \mathbf{C}_v}$, as it entails the derivative of the SVD. Fortunately, this derivative is published in [Papadopoulou and Lourakis \(2000\)](#).

4.3. Choice of parameters

The number of stiffness parameters of the torso model could be very large, with 6 different stiffness values per skeletal joint (the model has a total of 67 joints), and heterogeneous Lamé parameters in the soft tissue. While this may be appealing for reaching very high accuracy and personalization of the model, unfortunately the available measurement data does not provide sufficient information to estimate so many parameters, and the estimation could easily suffer from overfitting. We take a radically opposite approach, and minimize the number of estimated parameters necessary to obtain an accurate fit to the measurement data, while being robust to generalization to unseen deformations.

The study by [Koutras et al. \(2021\)](#) provides some insights to reduce the number of parameters while jointly maximizing accuracy and robustness. First, they suggest grouping the parameter ratios for some sets of vertebrae, e.g., all intervertebral joints share the same 6 parameter ratios for translation and rotation stiffness. It is important to highlight that, even though groups of joints share a common parameter ratio, the actual default parameters may be different as indicated in [Table 1](#). Second, [Koutras et al. \(2021\)](#) also show that only 6 parameters affect notably the deformation of the spine under three-point-pressure forces similar to those applied by scoliosis braces. In order of decreasing sensitivity, the parameters are: shear modulus or Lamé parameter μ , intervertebral lateral bending stiffness $k_{v,\gamma}$, intervertebral lateral translation stiffness $k_{v,x}$, intervertebral axial rotation stiffness $k_{v,\beta}$, intervertebral flexion/extension stiffness $k_{v,\alpha}$, and Lamé parameter λ . In our work, we have selected these same 6 parameters as tentative parameters for estimation.

However, as we discuss later in [Section 5.2](#), detailed sensitivity analysis of the objective gradient [\(10\)](#) under the measured data has shown that two terms of the gradient clearly dominate the rest, the terms corresponding to the shear modulus or Lamé parameter μ , and the intervertebral lateral bending stiffness $k_{v,\gamma}$. These were the main two parameters identified in [Koutras et al. \(2021\)](#) too. For robustness of the estimation, in practice we have limited the results to these two parameters, but we defer the reader to the full discussion in the next section.

4.4. Performance

One simulation (i.e., the computation of one static equilibrium deformation) can take up to 2 min, as it requires multiple iterations of a nonlinear Newton solver. One optimization process takes around 1 h, which in turn requires multiple deformation solves.

5. Results

We start this section by describing the subject data used in our experiments and tests. Then, we discuss the rationale for the final choice of estimated parameters, to maximize the robustness of the optimization. Next, we show the results of parameter estimation, validate them under test data, and compare the results to default stiffness parameters from the literature ([Ignasiak et al., 2015](#); [Koutras et al., 2021](#)). Finally, we provide a sensitivity analysis of the estimation procedure against errors in the measured forces.

5.1. Subjects and data

For this study, we obtained oral and written consent according to national guidelines and the Helsinki Declaration, and with approval of the local ethics committee of Hvidovre Hospital (No H-17034237). Seven subjects participated in the study. These were patients who had to be screened for scoliosis based on previous diagnosis or examination. Subject #7 should not be considered a scoliosis patient after all, and the other subjects would not undergo bracing in practice, based on the degree of their scoliosis. Nevertheless, this does not prevent the use of the stiffness estimation methodology.

[Table 2](#) lists the characteristics of the participants and the measured data. Four participants were female and three were male, with ages ranging 10 to 15 years. The average Cobb angle of the participants was 12.3 (± 3.2) degrees. The Cobb angle ([Safari et al., 2019](#)) is a common metric of scoliosis severity, as it measures the largest attainable angle between the superior endplate of a vertebra and the inferior endplate of some other vertebra. The maximum applied force on the ribs was on average 76.7 N (± 23 N). This produced an average change in Cobb angle of 22.4 (± 12) degrees, which quantifies the amount of deformation produced on the spine during the measurement procedure.

5.2. Selection of estimation parameters

Since the gradient of the objective function, $\frac{\partial f}{\partial \mathbf{k}}$ in [\(10\)](#), is expressed with respect to parameter ratios, the magnitude of each component of the gradient serves directly as a metric of sensitivity of each stiffness parameter. Therefore, to maximize the robustness of the parameter estimation, we have started by analyzing the gradient of the objective function with respect to tentative parameters. As announced in [Section 4.3](#), we have tentatively picked the 6 parameters highlighted by [Koutras et al. \(2021\)](#), namely: intervertebral lateral translation stiffness $k_{v,x}$, intervertebral flexion/extension stiffness $k_{v,\alpha}$, intervertebral axial rotation stiffness $k_{v,\beta}$, intervertebral lateral bending stiffness $k_{v,\gamma}$, Lamé parameter μ , and Lamé parameter λ .

[Table 3](#) shows the gradient of the objective function [\(10\)](#), for all 7 participants, with respect to these 6 parameters. Note that the actual values are not particularly relevant, but their ratios are. Two parameters clearly stand out: the Lamé parameter μ of the soft tissue, and the intervertebral lateral bending stiffness $k_{v,\gamma}$. In our parameter estimation, following the formulation in [Section 4](#), we consider only these two parameters. We have confirmed that adding the third most

Table 3

Gradient of the objective function (10), for all 7 participants, with respect to 6 tentative spine and torso stiffness parameters highlighted in previous work (Koutras et al., 2021). The translation and bending stiffness terms correspond all to the intervertebral joints, and the Lamé parameters correspond to the soft tissue. The comparison shows that 2 parameters clearly stand out: the shear modulus or Lamé parameter μ of the soft tissue, and the intervertebral lateral bending stiffness $k_{v,y}$. To maximize the robustness of the parameter estimation, we retain only these two parameters.

Parameter gradients	# 1	# 2	# 3	# 4	# 5	# 6	# 7	Average (abs)
Lateral translation $k_{v,x}$	110.5	85.8	113.8	143.4	10.6	60.3	21.0	77.9
Flexion/extension $k_{v,\alpha}$	-4.8	-44.9	-4.0	-3.1	-1.8	0.1	-4.4	9.0
Axial rotation $k_{v,\beta}$	66.0	207.6	114.8	185.6	10.4	41.1	14.9	91.5
Lateral bending $k_{v,y}$	1155.5	447.4	594.5	795.2	56.8	468.1	142.5	522.8
Lamé parameter μ	1821.1	688.4	695.3	1485.1	134.0	598.1	159.7	797.4
Lamé parameter λ	342.9	-152.3	25.7	305.2	4.6	72.2	-8.9	130.3

Table 4

Resulting values of the optimized parameter ratios, per patient. Note that these parameter ratios multiply the default stiffness parameters (obtained from the literature) listed in Table 1.

Optimized parameters	# 1	# 2	# 3	# 4	# 5	# 6	# 7	Average
Intervertebral lateral bending $k_{v,y}$	0.10	0.19	0.02	0.05	0.01	0.06	0.63	0.15
Lamé parameter μ	0.01	0.02	0.02	0.09	0.11	0.02	0.15	0.06

Table 5

RMSE (in mm) between measured image features and simulated results, across all patients. The RMSE is measured on the initial pose, the two training poses, and the validation pose. Note that our parameter estimation reduces the error, both in training and validation, to approximately 1/3, to a range comparable to the input skeleton geometry.

Fitting error	# 1	# 2	# 3	# 4	# 5	# 6	# 7	Average
Initial pose	1.55	3.87	2.09	2.56	2.99	2.13	1.56	2.39
Training poses, default params	15.08	10.88	14.27	11.67	4.62	9.68	3.37	9.94
Training poses, optimized params	3.54	4.53	4.12	3.87	2.95	1.95	2.45	3.35
Validation pose, default params	15.05	10.87	14.36	11.72	4.39	8.98	3.37	9.82
Validation pose, optimized params	3.29	4.43	4.13	3.99	3.00	1.93	2.37	3.30

Table 6

Comparison of Cobb angle (in deg), across patients: in the initial pose, in the validation pose (measured as a difference), simulated with default parameters, and simulation with estimated parameters. The average error in the validation pose is of 13.4 deg with default parameters, and just 2.9 deg with our estimated parameters.

Cobb angle	# 1	# 2	# 3	# 4	# 5	# 6	# 7	Average (abs)
Initial pose	+11	+16	+15	-10	+16	+11	+7	12.3
Diff in validation pose (measured)	-16	+6	-43	+26	0	-27	-15	19.0
Diff in validation pose (default params)	0	-1	-8	+16	-1	-3	-14	6.1
Diff in validation pose (optimized params)	-17	+4	-38	+30	+2	-25	-19	19.3

sensitive parameter to the optimization was not a positive choice. In 4 of the subjects, the optimization with 3 parameters led to extreme parameter values (and lack of simulation robustness), which is a clear indication of overfitting. In the other 3 subjects, the optimization error was reduced by only 3.6% with respect to the solution with just 2 parameters.

5.3. Optimization results

Table 4 shows the personalized values of the parameter ratios obtained by our optimization algorithm. Note that these parameter ratios multiply the default stiffness values obtained from the literature and listed in Table 1.

As discussed in Section 2.1, we have used two radiographs (and their corresponding forces) for parameter optimization, and one additional radiograph for validation. Table 5 lists the RMSE (in mm) between measured image features and the simulation results obtained by projecting the simulated vertebrae to the image plane (See Section 4.1 for the description of the full error computation procedure). Table 5 compares the error using the default stiffness parameters and our optimized parameters, in both the training poses and the validation pose. Table 5 also lists the error in the initial pose (with no applied force), which corresponds to the error of the geometry fitting algorithm (Koutras et al., 2022). Table 6 compares the change in Cobb angle between the initial rest pose and the validation pose in three cases: measured on the subjects, simulated with default parameters, and simulated with our estimated parameters. For reference, the table also

includes the Cobb angle of the subjects in the initial rest pose. Note that the actual Cobb angle may increase or decrease in the validation pose, depending on the direction in which the force was applied and the amount of force.

Figs. 4 and 5 provide qualitative visualization of the accuracy of the estimation. They illustrate the personalized models overlaid on the radiographs for the initial pose, the validation pose with default parameters, and the validation pose with optimized parameters. The figures also illustrate in all cases the target and simulated image features, which are used for error computation.

5.4. Sensitivity analysis

To conclude the experiments, we have analyzed the sensitivity of the estimated parameters with respect to potential errors produced e.g. by the measurement system prototype. To carry out this sensitivity analysis, we have varied the controlled force on the ribs F_3 by $\pm 10\%$, and we have re-estimated the stiffness parameters. Table 7 compiles the average change in the estimated parameters for each subject. The change is expressed as percentage with respect to our estimated parameter values.

6. Discussion

We start this final section with a discussion of the results. Then, we summarize the major conclusions resulting from our work. And we finish with a discussion of limitations and avenues for future work.

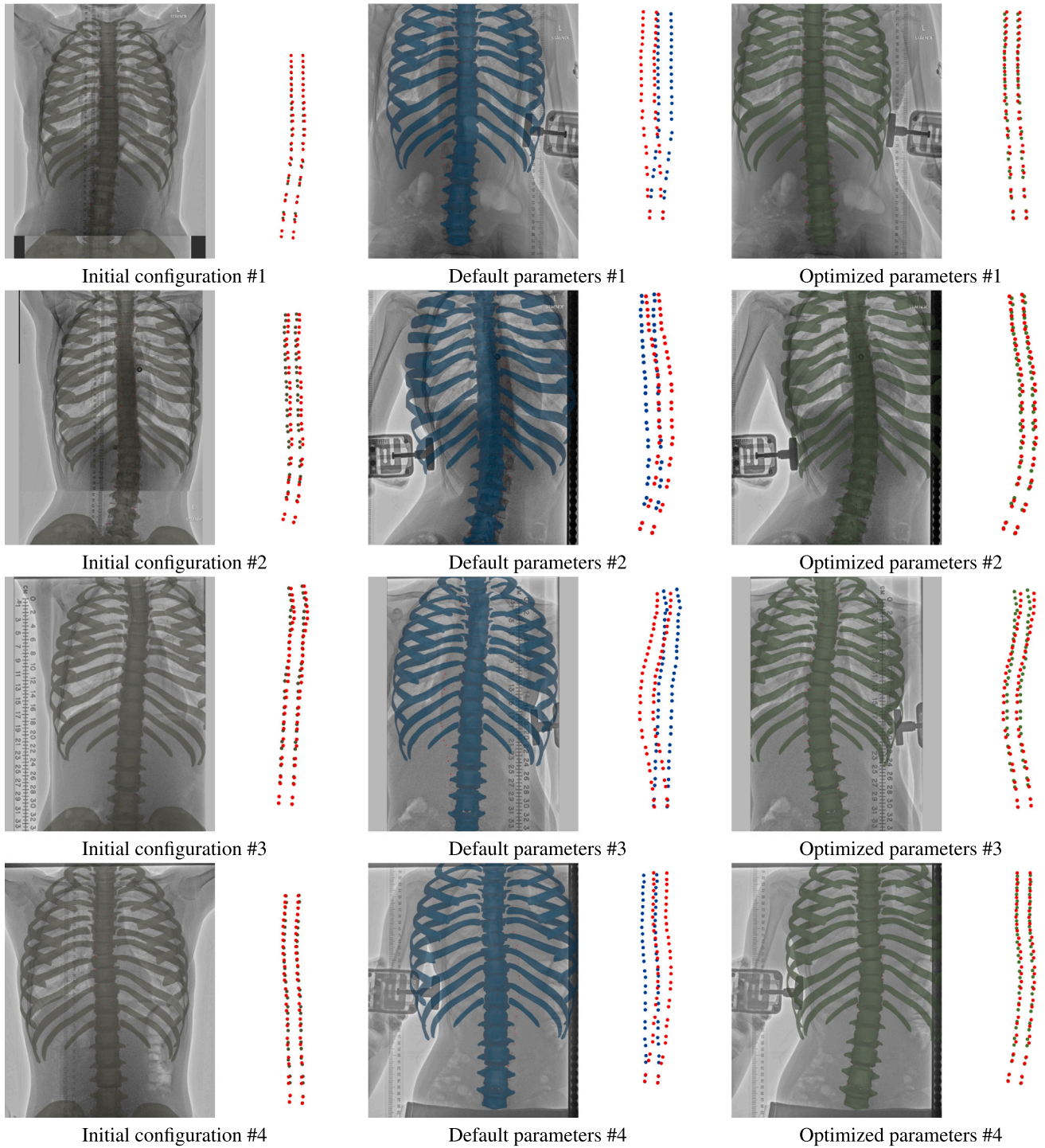


Fig. 4. Models of subjects 1–4 overlaid semitransparent on their corresponding radiographs, along with plots comparing tracked and simulated image features (i.e., vertebrae corners). Left: initial pose showing the input geometry fit. Middle: validation pose with default stiffness parameters. Right: validation pose with our optimized stiffness parameters.

Table 7

Sensitivity of estimated parameters to a 10% error in the measured forces. Measured as percentage with respect to our estimated parameter values.

Sensitivity of parameters	# 1	# 2	# 3	# 4	# 5	# 6	# 7	Average
Intervertebral lateral bending $k_{v,z}$	10.4%	7.9%	18.8%	0.0%	0.0%	13.8%	2.4%	7.6%
Lamé parameter μ	25.0%	44.4%	14.7%	27.8%	18.2%	40.0%	30.0%	28.6%

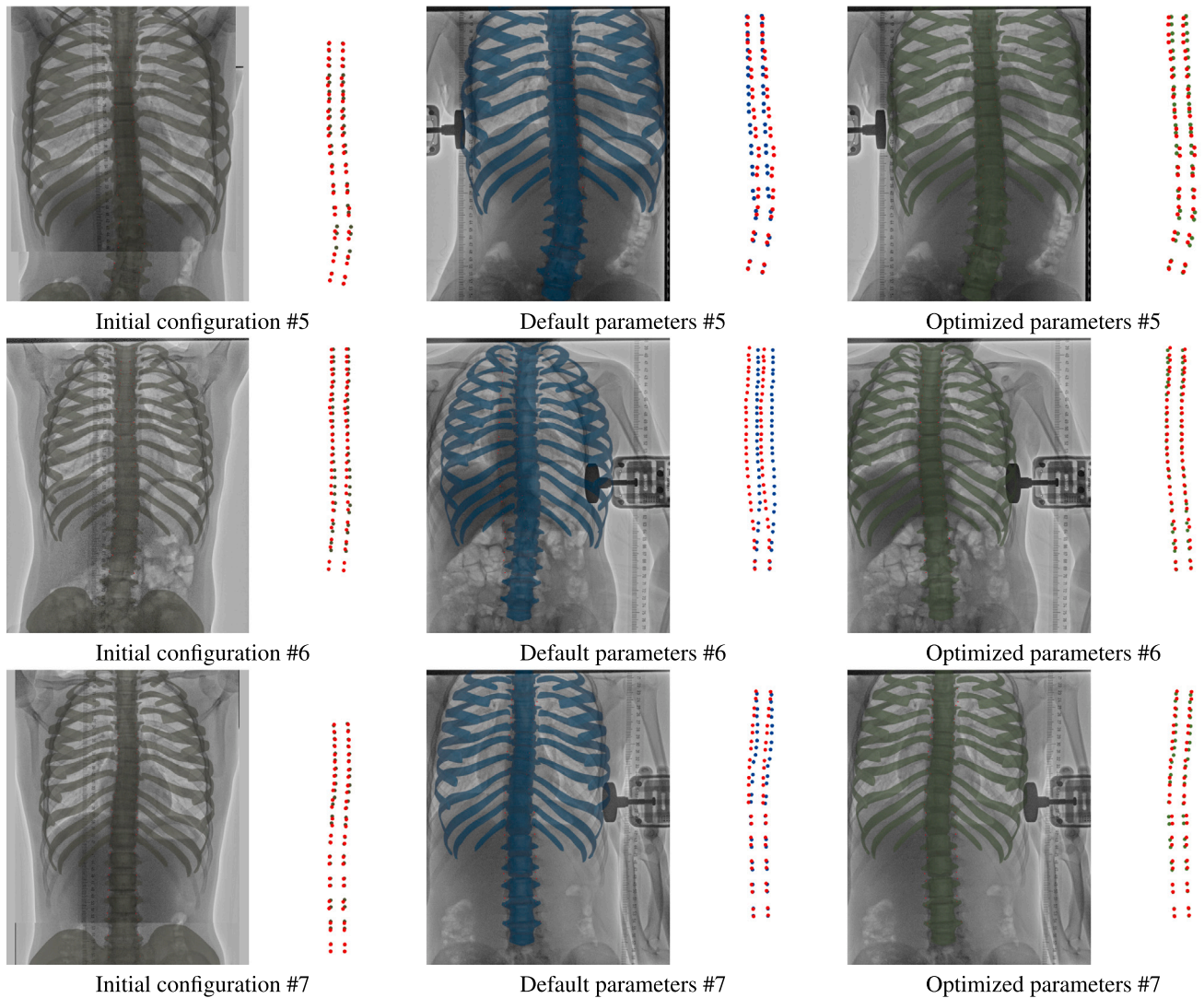


Fig. 5. Models of subjects 5–7 overlaid semitransparent on their corresponding radiographs, along with plots comparing tracked and simulated image features (i.e., vertebrae corners). Left: initial pose showing the input geometry fit. Middle: validation pose with default stiffness parameters. Right: validation pose with our optimized stiffness parameters.

6.1. Discussion of results

From the estimated parameters in Table 4, we observe that the default parameters are considerably stiffer (up to two orders of magnitude in some cases) than the personalized parameters for all participants.

From the image-fitting error data in Table 5, we can draw several significant observations:

1. On the training poses, our parameter optimization method achieves a reduction of the error to 1/3 of the error with default stiffness parameters. Quantitatively, this means a reduction from an RMSE of approx. 10 mm to 3.35 mm.
2. Very similar error reduction is achieved on the validation pose, demonstrating that the results generalize to other applied forces.
3. The error achieved by the parameter optimization is very similar to the error present in the initial pose. Note that the initial pose sets an upper bound on the accuracy of the parameter estimation; this can never achieve higher accuracy than that of the initial geometry. Adding more parameters to the optimization could decrease the error even below the initial error, but this would be a sign of overfitting.
4. As hypothesized, there is an evident correspondence between the absolute RMSE (Table 5) and the spine and torso stiffness (Table 4) across the participants. The models of stiffer participants (e.g., subject 7) show considerably lower error.
5. The results are robust to the diversity in the participants and the measured data (i.e., male and female, left and right scoliosis curvature, increased and decreased curvature during measurements). Note that the error improvement with respect to default parameters shows a very similar trend across all participants.

From the Cobb angle data in Table 6, we draw similar observations:

- The average error in Cobb angle in the validation pose is 4.6× higher with default parameters than with the estimated parameters. This average error is reduced from 13.4 degrees to just 2.9 degrees. Note that the maximum error with our estimated parameters is of just 5 degrees, and this is on cases with large deformation with respect to the initial pose.
- Similar to the image-fitting error, there is a correspondence between the Cobb-angle error with default parameters and the actual spine stiffness of the subjects, with stiffer subjects showing less error.

Last, the sensitivity data in Table 7 indicates that the estimated Lamé parameter μ is notably more sensitive to measurement error than the intervertebral lateral bending stiffness. While the latter is rather robust (sensitivity below 1), the former shows a high sensitivity (average of almost 3).

6.2. Conclusions

The results of our study allow us to draw several conclusions about modeling and characterization of spine and torso stiffness for scoliosis bracing design.

- The results confirm our initial hypothesis: personalized stiffness values are considerably lower than the default values in the bibliography. This is no surprise, as the default values are derived from *in-vitro* experiments on cadavers of mature subjects, while we performed *in-vivo* experiments on adolescent subjects.
- Based on the range of the optimized parameters, personalized biomechanical models are necessary for accurately capturing the spine's mechanical response, specially for personalized computational brace design.
- Intervertebral lateral bending stiffness and shear modulus of the soft tissue explain the majority of the personalized response in lateral bending deformations relevant for scoliosis bracing.
- Modeling the soft tissue in the skeleton is key for a correct characterization. Furthermore, the high sensitivity of the Lamé parameter μ to force measurement errors indicates that correct characterization of the soft-tissue stiffness requires even more care than characterization of the spine stiffness.

We also draw conclusions about the proposed methodology for stiffness characterization.

- Given the low error in vertebrae positions (below 3.3 mm) under validation conditions not used for training, we can conclude that the resulting personalized biomechanical models succeed to reproduce the force–deformation response under conditions that mimic spinal bracing.
- Using force data for the parameter estimation, together with the inverse-modeling optimization approach, are key elements for the success of the proposed methodology.
- The low encumbrance of the proposed system for force-and-deformation data acquisition makes the overall methodology suitable for implementation in the clinical protocol for computational design of spinal braces for AIS.
- The differentiable biomechanics model and the optimization-based estimation algorithm succeed in reaching stiffness parameters that are accurate yet robust, i.e., they do not suffer overfitting.

6.3. Limitations and future work

Our methodology and results suggest multiple avenues of future work. Some could overcome the technical limitations of our current proposal, while others could explore its clinical impact.

The validation of the estimated parameters was executed using forces applied at the same locations as those used for estimation, and this limits the validation of the generalization capabilities of the resulting models. One possible improvement could be to use more general force–deformation data, both for estimation and for validation, with forces applied at different locations on the ribs. However, this is not free of challenges, as increasing the amount of data would increase the radiation exposure on the subjects. One way to increase the amount of data could be to combine some radiograph images with images of markers on the surface of the torso. Another possible improvement could be to use force–deformation data that is closer to the conditions

imposed by braces, leveraging expert knowledge of the clinicians to define force location and range differently for each subject. One such approach could be to fix the torso at the axilla and not at the shoulder, but this would require building a more complicated support system.

The measurement prototype lacks some robustness, and as a result we discarded data where the shoulder or the pelvis did not remain fully fixed in practice. A revision of the prototype should focus on building dedicated fixation elements to guarantee higher robustness. In addition to lack of measurement robustness, another possible source of error is undetected external forces, such as in the back or the feet. New iterations of the measurement prototype could include quantification and minimization of these forces.

In AIS, spinal curvature is correlated to axial rotation (Easwar et al., 2011). For this reason, modern brace designs aim to correct both lateral bending and axial rotation. Our proposed methodology is focused on measurement and personalization of the lateral bending behavior, and it should be extended to include representative axial rotation data for larger generality. While our results only reveal sensitivity of the intervertebral lateral bending stiffness and the shear modulus of soft tissue, perhaps the inclusion of axial rotation data could point to the relevance of other stiffness parameters such as intervertebral axial rotation stiffness. Obtaining axial rotation data is however nontrivial, as it would require the acquisition of 3D deformations using, e.g., biplanar radiographs, but we have already mentioned the risk of increased radiation exposure.

All in all, while the current results of our methodology are very promising, its implementation on clinical settings requires more extended validation, covering a larger cohort and subjects with more severe scoliosis. It is also necessary to identify if the model personalization provided by the methods is sufficient for the application of computational brace design in practice, or if higher accuracy is needed. If higher accuracy is actually needed, this could come from improvements to the estimation methodology, but also to the underlying parameterization of the biomechanical model. Possible extensions to the model include making the soft tissue heterogeneous, adding more complex models for joints, or adding muscle forces. However, increasing the parameter space of the model makes parameter estimation ever more complex, and our experiments already emphasize the risk of parameter overfitting.

Beyond the application to computational brace design, the estimation of personalized stiffness response of the torso and the spine could also be relevant for the clinical study of AIS. Estimating the stiffness parameters for a larger cohort would open the door to analyzing possible correlations to age, height, gender, and degree and progression of scoliosis. And, ultimately, this might allow novel investigation on the aetiology of scoliosis

To conclude, we remark that our measurement and estimation methodology target the personalization of the stiffness response of the torso and the spine for AIS-related applications. While the results are not general enough for comprehensive modeling of the torso and the spine, the methodology features several elements that could be applied in the context of comprehensive modeling, such as the acquisition of combined force–deformation data, the development of a differentiable biomechanical model, and the design of an optimization procedure built on differentiability of both biomechanics and the data acquisition process.

CRedit authorship contribution statement

Christos Koutras: Writing – original draft, Visualization, Validation, Software, Methodology, Investigation, Formal analysis, Data curation, Conceptualization. **Hamed Shayestehpour:** Writing – review & editing, Data curation, Conceptualization. **Jesús Pérez:** Writing – review & editing, Software, Methodology, Conceptualization. **Christian Wong:** Writing – review & editing, Resources, Data curation, Conceptualization. **John Rasmussen:** Writing – review & editing, Conceptualization. **Miguel A. Otaduy:** Writing – original draft, Visualization, Validation, Supervision, Resources, Project administration, Methodology, Funding acquisition, Formal analysis, Conceptualization.

Ethical approval

All data used in this paper was provided, already anonymized, by the University Hospital of Hvidovre, and was obtained with oral and written consent from the patients according to national Danish guidelines and the Helsinki declaration, and with approval of the local ethics committee (No H-17034237).

Funding

This project has received funding from the European Union's Horizon 2020 research and innovation programme under the Marie Skłodowska-Curie grant agreement No. 764644, Rainbow. This paper only contains the author's views and the Research Executive Agency and the Commission are not responsible for any use that may be made of the information it contains.

Declaration of competing interest

The authors declare that they have no known competing financial interests or personal relationships that could have appeared to influence the work reported in this paper.

Acknowledgments

The authors would like to thank Anna Arnesen, Faezeh Moshfeghifar, Thomas Alscher and Mathias Højgaard Jensen for their help with the acquisition process; Cristian Romero, Zhongyun He and Igor Santesteban for their help with the rendering pipeline. Finally, the authors would like to thank the rest of the members of the MSLab at URJC for their support.

Appendix A. Supplementary data

Supplementary material related to this article can be found online at <https://doi.org/10.1016/j.media.2025.103573>.

Data availability

The authors do not have permission to share data.

References

- Affolter, C., Kedzierska, J., Vielma, T., Weisse, B., Aiyangar, A., 2020. Estimating lumbar passive stiffness behaviour from subject-specific finite element models and in vivo 6DOF kinematics. *J. Biomech.* 102, 109681. <http://dx.doi.org/10.1016/j.jbiomech.2020.109681>, URL: <https://www.sciencedirect.com/science/article/pii/S002192902030097X> 3rd International Workshop on Spine Loading and Deformation.
- Alizadeh, M., Knapik, G.G., Mageswaran, P., Mendel, E., Bourekas, E., Marras, W.S., 2020. Biomechanical musculoskeletal models of the cervical spine: A systematic literature review. *Clin. Biomech.* 71, 115–124.
- Bayoglu, R., Galibarov, P.E., Verdonshot, N., Koopman, B., Homminga, J., 2019. Twente spine model: A thorough investigation of the spinal loads in a complete and coherent musculoskeletal model of the human spine. *Med. Eng. Phys.* 68, 35–45.
- Berger, S., Marcello, O., Schuman, S., Schneider, J., Studer, D., Hasler, C., Zheng, G., Büchler, P., 2015. Patient-specific spinal stiffness in AIS: a preoperative and noninvasive method. *Eur. Spine J.* 24 (2), 249–255.
- Bickel, B., Bächer, M., Otaduy, M.A., Matusik, W., Pfister, H., Gross, M., 2009. Capture and modeling of non-linear heterogeneous soft tissue. *ACM Trans. Graph.* 28 (3).
- Bisschop, A., Mullender, M.G., Kingma, I., Jiya, T.U., van der Veen, A.J., Roos, J.C., van Dieën, J.H., van Royen, B.J., 2012. The impact of bone mineral density and disc degeneration on shear strength and stiffness of the lumbar spine following laminectomy. *Eur. Spine J.*
- Bradski, G., 2000. The OpenCV Library. Dr. Dobb's J. Softw. Tools.
- Büchler, P., de Oliveria, M.E., Studer, D., Schumann, S., Zheng, G., Schneider, J., Hasler, C.C., 2014. Axial suspension test to assess pre-operative spinal flexibility in patients with adolescent idiopathic scoliosis. *Eur. Spine J.* 23 (12), 2619–2625.
- Clin, J., Aubin, C.E., Sangole, A., Labelle, H., Parent, S., 2010. Correlation between immediate in-brace correction and biomechanical effectiveness of brace treatment in adolescent idiopathic scoliosis. *Spine* 35 (18), 1706–1713.
- Cobetto, N., Aubin, C.-É., Parent, S., Barchi, S., Turgeon, I., Labelle, H., 2017. 3D correction of AIS in braces designed using CAD/CAM and FEM: a randomized controlled trial. *Scoliosis Spinal Disord.* 12 (1), 1–8.
- Courvoisier, A., Nesme, M., Gerbelot, J., Moreau-Gaudry, A., Faure, F., 2019. Prediction of brace effect in scoliotic patients: blinded evaluation of a novel brace simulator-an observational cross-sectional study. *Eur. Spine J.* 28 (6), 1277–1285.
- de Zee, M., Hansen, L., Wong, C., Rasmussen, J., Simonsen, E.B., 2007. A generic detailed rigid-body lumbar spine model. *J. Biomech.* 40, 1219–1227.
- Dicko, A.H., Tong-Yette, N., Gilles, B., Faure, F., Palombi, O., 2015. Construction and validation of a hybrid lumbar spine model for the fast evaluation of intradiscal pressure and mobility. *World Acad. Sci. Eng. Technol.*
- Dong, E., Shi, L., Kang, J., Li, D., Liu, B., Guo, Z., Wang, L., Li, X., 2020. Biomechanical characterization of vertebral body replacement in situ: Effects of different fixation strategies. *Comput. Methods Programs Biomed.* 105741.
- Easwar, T., Hong, J.-Y., Yang, J.H., Suh, S.W., Modi, H.N., 2011. Does lateral vertebral translation correspond to Cobb angle and relate in the same way to axial vertebral rotation and rib hump index? A radiographic analysis on idiopathic scoliosis. *Eur. Spine J.* 20 (7), 1095–1105.
- Eskandari, A., Arjmand, N., Shirazi-Adl, A., Farahmand, F., 2017. Subject-specific 2D/3D image registration and kinematics-driven musculoskeletal model of the spine. *J. Biomech.* 57, 18–26.
- Favier, C., Finnegan, M., Quest, R., Honeyfield, L., McGregor, A., Phillips, A., 2021. An open-source musculoskeletal model of the lumbar spine and lower limbs: a validation for movements of the lumbar spine. *Comput. Methods Biomech. Biomed. Eng.* 24 (12), 1310–1325.
- Ghezl bash, F., Shirazi-Adl, A., Arjmand, N., El-Ouaaid, Z., Plamondon, A., 2016. Subject-specific biomechanics of trunk: musculoskeletal scaling, internal loads and intradiscal pressure estimation. *Biomech. Model. Mechanobiol.* 15 (6), 1699–1712.
- Gignac, D., Aubin, C.-É., Dansereau, J., Labelle, H., 2000. Optimization method for 3D bracing correction of scoliosis using a finite element model. *Eur. Spine J.* 9 (3), 185–190.
- Gould, S.L., Cristofolini, L., Davico, G., Viceconti, M., 2021. Computational modelling of the scoliotic spine: A literature review. *Int. J. Numer. Methods Biomed. Eng.* 37 (10), e3503.
- Guennebaud, G., Jacob, B., et al., 2010. Eigen v3. <http://eigen.tuxfamily.org>.
- Guy, A., Aubin, C.-E., 2023. Finite element simulation of growth modulation during brace treatment of adolescent idiopathic scoliosis. *J. Orthop. Res.* 41 (9), 2065–2074.
- Guy, A., Labelle, H., Barchi, S., Audet-Duchesne, E., Cobetto, N., Parent, S., Raison, M., Aubin, C.-É., 2021. Braces designed using CAD/CAM combined or not with finite element modeling lead to effective treatment and quality of life after 2 years: A randomized controlled trial. *Spine* 46 (1), 9–16.
- Hang, S., 2015. TetGen, a delaunay-based quality tetrahedral mesh generator. *ACM Trans. Math. Software* 41 (2), 11.
- Ignasiak, D., Dendorfer, S., Ferguson, S.J., 2015. Thoracolumbar spine model with articulated rib cage for the prediction of dynamic spinal loading. *J. Biomech.*
- Jalalian, A., Gibson, I., Tay, E.H., 2013. Computational biomechanical modeling of scoliotic spine: challenges and opportunities. *Spine Deform.* 1 (6), 401–411.
- Jalalian, A., Tay, F.E., Arastehfar, S., Liu, G., 2017. A new method to approximate load-displacement relationships of spinal motion segments for patient-specific multi-body models of scoliotic spine. *Med. Biol. Eng. Comput.* 55 (6), 1039–1050.
- Kaelin, A.J., 2020. Adolescent idiopathic scoliosis: indications for bracing and conservative treatments. *Ann. Transl. Med.* 8 (2).
- Kardash, K., Koutras, C., Otaduy, M.A., 2022. Design of personalized scoliosis braces based on differentiable biomechanics—Synthetic study. *Front. Bioeng. Biotechnol.* 10, <http://dx.doi.org/10.3389/fbioe.2022.1014365>, URL: <https://www.frontiersin.org/articles/10.3389/fbioe.2022.1014365>.
- Knapik, G.G., Mendel, E., Bourekas, E., Marras, W.S., 2022. Computational lumbar spine models: A literature review. *Clin. Biomech.* 105816.
- Koutras, C., Pérez, J., Kardash, K., Otaduy, M.A., 2021. A study of the sensitivity of biomechanical models of the spine for scoliosis brace design. *Comput. Methods Programs Biomed.* 207, 106125.
- Koutras, C., Shayestehpour, H., Pérez, J., Wong, C., Rasmussen, J., Tournier, M., Nesme, M., Otaduy, M.A., 2022. Biomechanical morphing for personalized fitting of scoliotic torso skeleton models. *Front. Bioeng. Biotechnol.* 1238.
- Kuroki, H., 2018. Brace treatment for adolescent idiopathic scoliosis. *J. Clin. Med.* 7 (6), 136.
- Lafon, Y., Lafage, V., Steib, J.-P., Dubouset, J., Skalli, W., 2010. In vivo distribution of spinal intervertebral stiffness based on clinical flexibility tests. *Spine* 35 (2), 186–193.
- Lasswell, T.L., Cronin, D.S., Medley, J.B., Rasoulinejad, P., 2017. Incorporating ligament laxity in a finite element model for the upper cervical spine. *Spine J.* 17 (11), 1755–1764.
- Liebsch, C., Graf, N., Appelt, K., Wilke, H.-J., 2017. The rib cage stabilizes the human thoracic spine: An in vitro study using stepwise reduction of rib cage structures. *PLoS One* 12 (6), e0178733.
- Liebsch, C., Graf, N., Wilke, H.-J., 2019. In vitro analysis of kinematics and elastostatics of the human rib cage during thoracic spinal movement for the validation of numerical models. *J. Biomech.* 94, 147–157.
- Lions, J.L., 1971. *Optimal Control of Systems Governed by Partial Differential Equations*. Springer-Verlag, New York.

- McNamara, A., Treuille, A., Popović, Z., Stam, J., 2004. Fluid control using the adjoint method. *ACM Trans. Graph.* 23 (3), 449–456.
- Miguel, E., Bradley, D., Thomaszewski, B., Bickel, B., Matusik, W., Otaduy, M.A., Marschner, S., 2012. Data-driven estimation of cloth simulation models. *Comput. Graph. Forum* 31 (2pt2), 519–528.
- Moroney, S.P., Schultz, A.B., Miller, J.A., Andersson, G.B., 1988. Load-displacement properties of lower cervical spine motion segments. *J. Biomech.* 21 (9), 769–779.
- Murray, R.C., Ophaswongse, C., Park, J.-H., Agrawal, S.K., 2020. Characterizing torso stiffness in female adolescents with and without scoliosis. *IEEE Robot. Autom. Lett.* 5 (2), 1634–1641.
- Naoum, S., Vasiliadis, A.V., Koutserimpas, C., Mylonakis, N., Kotsapas, M., Katakalos, K., 2021. Finite element method for the evaluation of the human spine: A literature overview. *J. Funct. Biomater.* 12 (3), 43.
- Nie, W.-Z., Ye, M., Liu, Z.-D., Wang, C.-T., 2009. The patient-specific brace design and biomechanical analysis of adolescent idiopathic scoliosis. *J. Biomech. Eng.* 131 (4).
- Nocedal, J., Wright, S.J., 2006. Quadratic programming. *Numer. Optim.* 448–492.
- Ogden, R., 1997. *Non-linear Elastic Deformations*. Dover Publications.
- Panjabi, M.M., Brand Jr., R.A., White III, A.A., 1976. Three-dimensional flexibility and stiffness properties of the human thoracic spine. *J. Biomech.* 9 (4), 185–192.
- Panjabi, M.M., Oxland, T., Yamamoto, I., Crisco, J.J., 1994. Mechanical behavior of the human lumbar and lumbosacral spine as shown by three-dimensional load-displacement curves. *J. Bone Jt. Surg. Am. Vol.* 76 (3), 413–424.
- Papadopoulou, T., Lourakis, M.I., 2000. Estimating the jacobian of the singular value decomposition: Theory and applications. In: *European Conference on Computer Vision*. Springer, pp. 554–570.
- Park, J.-H., Stegall, P.R., Roye, D.P., Agrawal, S.K., 2018. Robotic spine exoskeleton (RoSE): Characterizing the 3-d stiffness of the human torso in the treatment of spine deformity. *IEEE Trans. Neural Syst. Rehabil. Eng.* 26 (5), 1026–1035.
- Pérez, J., Otaduy, M.A., Thomaszewski, B., 2017. Computational design and automated fabrication of Kirchhoff-plateau surfaces. *ACM Trans. Graph.* 36 (4).
- Pérez, J., Thomaszewski, B., Coros, S., Bickel, B., Canabal, J.A., Sumner, R., Otaduy, M.A., 2015. Design and fabrication of flexible rod meshes. *ACM Trans. Graph.* 34 (4).
- Petit, Y., Aubin, C.-É., Labelle, H., 2004. Patient-specific mechanical properties of a flexible multi-body model of the scoliotic spine. *Med. Biol. Eng. Comput.* 42 (1), 55–60.
- Qiao, G., Rahmatalla, S., 2020. Identification of damping and stiffness parameters of cervical and lumbar spines of supine humans under vertical whole-body vibration. *J. Low Freq. Noise, Vib. Act. Control.* 39 (1), 59–71.
- Rasmussen, J., 2019. The AnyBody modeling system. *DHM Posturography* 85–96.
- Rigo, M., Jelačić, M., 2017. Brace technology thematic series: the 3D rigo chèneau-type brace. *Scoliosis Spinal Disord.* 12 (1), 1–46.
- Safari, A., Parsaei, H., Zamani, A., Pourabbas, B., 2019. A semi-automatic algorithm for estimating Cobb angle. *J. Biomed. Phys. Eng.* 9 (3), 317.
- Schmid, S., Burkhart, K.A., Allaire, B.T., Grindle, D., Anderson, D.E., 2020. Musculoskeletal full-body models including a detailed thoracolumbar spine for children and adolescents aged 6–18 years. *J. Biomech.* 102, 109305.
- Shayestehpour, H., Rasmussen, J., Galibarov, P., Wong, C., 2021. An articulated spine and ribcage kinematic model for simulation of scoliosis deformities. *Multibody Syst. Dyn.* 1–20.
- Sifakis, E., Barbic, J., 2012. FEM simulation of 3D deformable solids: a practitioner's guide to theory, discretization and model reduction. In: *Acm Siggraph 2012 Courses*. pp. 1–50.
- Smith, B., Goes, F.D., Kim, T., 2018. Stable neo-hookean flesh simulation. *ACM Trans. Graph.* 37 (2), 1–15.
- Taylor, C.J., Kriegman, D.J., 1994.
- Vergari, C., Chen, Z., Robichon, A., Courtois, I., Ebermeyer, E., Vialle, R., Langlais, T., Pietton, R., Skalli, W., 2020. Towards a predictive simulation of brace action in adolescent idiopathic scoliosis. *Comput. Methods Biomech. Biomed. Eng.* 1–8.
- Virtanen, P., Gommers, R., Oliphant, T.E., Haberland, M., Reddy, T., Cournapeau, D., Burovski, E., Peterson, P., Weckesser, W., Bright, J., van der Walt, S.J., Brett, M., Wilson, J., Millman, K.J., Mayorov, N., Nelson, A.R.J., Jones, E., Kern, R., Larson, E., Carey, C.J., Polat, İ., Feng, Y., Moore, E.W., VanderPlas, J., Laxalde, D., Perktold, J., Cimrman, R., Henriksen, I., Quintero, E.A., Harris, C.R., Archibald, A.M., Ribeiro, A.H., Pedregosa, F., van Mulbregt, P., SciPy 1.0 Contributors, 2020. *SciPy 1.0: Fundamental Algorithms for Scientific Computing in Python*. *Nature Methods* 17, 261–272. <http://dx.doi.org/10.1038/s41592-019-0686-2>.
- Wang, W., Baran, G.R., Betz, R.R., Samdani, A.F., Pahys, J.M., Cahill, P.J., 2014. The use of finite element models to assist understanding and treatment for scoliosis: a review paper. *Spine Deform.* 2 (1), 10–27.
- Wang, W., Wang, D., Falisse, A., Severijns, P., Overbergh, T., Moke, L., Scheys, L., De Groote, F., Jonkers, I., 2021. A dynamic optimization approach for solving spine kinematics while calibrating subject-specific mechanical properties. *Ann. Biomed. Eng.* 49 (9), 2311–2322.
- Wei, W., Zhang, T., Huang, Z., Yang, J., 2022. Finite element analysis in brace treatment on adolescent idiopathic scoliosis. *Med. Biol. Eng. Comput.* 1–14.
- Wilke, H.-J., Herkammer, A., Werner, K., Liebsch, C., 2017. In vitro analysis of the segmental flexibility of the thoracic spine. *PLoS One* 12 (5), e0177823.
- Wojtan, C., Mucha, P.J., Turk, G., 2006. Keyframe Control of Complex Particle Systems Using the Adjoint Method. In: *Cani, M.-P., O'Brien, J. (Eds.), ACM SIGGRAPH / Eurographics Symposium on Computer Animation*. The Eurographics Association.
- Wong, C., Adriansen, J., Jeppsen, J., Balslev-Clausen, A., 2021. Intervariability in radiographic parameters and general evaluation of a low-dose fluoroscopic technique in patients with idiopathic scoliosis. *Acta Radiol. Open* 10 (9).
- Wright, S., Nocedal, J., et al., 1999. *Numerical optimization*. Springer Sci. 35 (67–68), 7.
- Xu, M., Yang, J., Lieberman, I.H., Haddas, R., 2017. Lumbar spine finite element model for healthy subjects: development and validation. *Comput. Methods Biomech. Biomed. Eng.* 20 (1), 1–15.
- Yamamoto, S., Dias, L., Street, J., Crompton, P.A., Oxland, T.R., 2022. Anteroposterior shear stiffness of the upper thoracic spine at quasi-static and dynamic loading rates—An in vitro biomechanical study. *J. Orthop. Res.* textregistered 40 (7), 1687–1694.
- Zhang, C., Mannen, E.M., Sis, H.L., Cadel, E.S., Wong, B.M., Wang, W., Cheng, B., Friis, E.A., Anderson, D.E., 2020. Moment-rotation behavior of intervertebral joints in flexion-extension, lateral bending, and axial rotation at all levels of the human spine: A structured review and meta-regression analysis. *J. Biomech.* 100, 109579. <http://dx.doi.org/10.1016/j.jbiomech.2019.109579>, URL: <https://www.sciencedirect.com/science/article/pii/S0021929019308425>.
- Zhao, D., Li, Y., Chaudhuri, S., Langlois, T., Barbic, J., 2022. ERGOBOSS: onomic optimization of dy-upporting urfaces. *IEEE Trans. Vis. Comput. Graphics* 28 (12), 4032–4047.

Christos Koutras is a Ph.D. fellow in the Multimodal Simulation Lab (MSLab) in the Department of Computer Science of URJC and Rainbow, a Marie Skłodowska-Curie European Training Network. He obtained his Diploma in the Aristotle University of Thessaloniki (AUTH) in the Department of Mechanical Engineering in 2017. In 2018 he was working as a Research Assistant in the Machine Dynamics lab of AUTH. Currently, he is researching spine biomechanics. His goal is to develop a pipeline which will produce fully personalized models of the torso biomechanics of AIS patients, which will be later used for scoliosis brace design.

Hamed Shayestehpour received his BS and MS degrees in Mechanical Engineering from Sharif University of Technology, Tehran, Iran in 2015 and 2017, respectively. His research interests include biomechanics, biomedical engineering, simulations and modeling. Since 2019, he is a Ph.D. fellow at Aalborg university, and Rainbow, a Marie Skłodowska-Curie European Training Network. His Ph.D. is aimed at comprehensive musculoskeletal modeling of adolescent idiopathic scoliosis to help understanding aetiology and biomechanics behind it. Currently, he is working at AnyBody Technology A/S as a part-time Biomechanics Specialist alongside his Ph.D. project.

Jesus Perez is an enthusiast of software development, computer graphics, and artificial intelligence. He holds a Ph.D. degree in Computer Graphics and his research focused on physics-based animation and related application fields, such as data-driven materials, computational design, and digital fabrication. Currently, his interests lie in high-performance biomechanical simulation, model reduction, and simulation enrichment using deep learning.

Christian Wong is a full-time consultant at the children's section, the National University Hospital, Copenhagen, Denmark. He is chairman of the Danish (2017) and European pediatric orthopaedic research society (2022), respectively. He is a member of the specialist council in the national patient organization 'CP Danmark', and the national and regional board for the national database for children with CP, CPOP (2021).

John Rasmussen is a professor of biomechanics at Aalborg University. As one of the original inventors of the AnyBody Modeling System, he works on biomechanics in general with a special focus on multibody musculoskeletal analysis methods. The typical applications are diverse, for instance in orthopaedics, industrial design, ergonomics, and sports science. He also has interests in tissue engineering, computeraided engineering, computer-aided design, and design optimization.

Miguel A. Otaduy is full professor of computer science and director of the Multimodal Simulation Lab at Universidad Rey Juan Carlos, and also research scientist at Meta Reality Labs Research. He holds a BS (2000) in Electrical Engineering from Mondragon University, and MS (2003) and Ph.D. (2004) in Computer Science from the University of North Carolina at Chapel Hill. From 2005 to 2008, he was research associate at ETH Zurich, and from 2017 to 2022 chief science officer at SEDDI. He is a recipient of ERC.